Influence of defects on structural and magnetic properties of multifunctional La_2NiMnO_6 thin films

H. Z. Guo, J. Burgess, E. Ada, S. Street, and A. Gupta*
Center for Materials for Information Technology and Department of Chemistry, University of Alabama, Tuscaloosa, Alabama 35487, USA

M. N. Iliev
Texas Center for Superconductivity and Department of Physics, University of Houston, Houston, Texas 77204, USA

A. J. Kellock
IBM Corporation, Almaden Research Center, San Jose, California 95120, USA

C. Magen, M. Varela, and S. J. Pennycook
Oak Ridge National Laboratory, Oak Ridge, Tennessee 37831, USA
(Received 6 November 2007; revised manuscript received 22 March 2008; published 16 May 2008)

Thin films of the double perovskite La_2NiMnO_6 (LNMO) have been grown on various lattice-matched substrates ($SrTiO_3$, $LaAlO_3$, $NdGaO_3$, and MgO) by pulsed laser deposition under different oxygen background pressure (25–800 mTorr) conditions. The out-of-plane lattice constant of the LNMO film decreases with increasing pressure, which is likely caused by reduction in the defect concentration and improved structural ordering, before leveling off at higher oxygen concentrations. The scanning transmission electron microscopy results confirm that the films are epitaxial, and the interface is sharp and coherent. While few defects are observed in a film grown at a high oxygen pressure (800 mTorr), a film grown at a lower pressure (100 mTorr) clearly shows the formation of defects that extend throughout the thickness except for a very thin layer near the interface. The Raman spectra of the films are dominated by two broad peaks at around 540 and 685 cm^{-1}, which are assigned to the antisymmetric stretching and symmetric stretching modes of MnO_6 and NiO_6 octahedra, respectively. The Raman peaks of the LNMO thin films grown in the 800 mTorr background O_2 are blueshifted in comparison to those of bulk LNMO, and the shift increases with decreasing film thickness, indicating the increased influence of strain. The critical thickness for strain relaxation, as determined from the Raman spectra, is between 40 and 80 nm. However, the strain is observed to have negligible influence on the magnetic properties of films grown at high oxygen pressures. In contrast, films grown at low pressures exhibit degraded magnetic properties, which can be attributed to a combination of increased *B*-site cation disorder and the concentration of Mn^{3+} and Ni^{3+} Jahn-Teller ions caused by oxygen or cation related defects. With increasing oxygen pressure during growth, the paramagnetic-ferromagnetic transition temperature (~280 K) becomes sharper and the saturation magnetization at low temperatures is enhanced. Based on the electron energy loss spectroscopy studies, the Mn and Ni ions in LNMO thin films are determined to be mixed-valent Mn^{3+}/Mn^{4+}, and charge transition disproportionation of the $Mn^{4+}+Ni^{2+} \rightarrow Mn^{3+}+Ni^{3+}$ type likely occurs with increasing oxygen deficiency.

DOI: 10.1103/PhysRevB.77.174423 PACS number(s): 77.84.Dy, 61.66.−f, 75.70.−i, 68.55.−a

I. INTRODUCTION

In recent years, there has been resurgence of interest in multifunctional materials that simultaneously possess electric and magnetic orderings, which is driven in a large part by the ever increasing need for lower power consumption and additional functionality for next-generation electronic devices.[1–7] A large magnetoelectric (ME) coupling effect is needed for practical applications, but the intrinsic coupling strength observed thus far in multifunctional materials has typically been quite small. Recent discoveries of a giant ME effect in $RMnO_3$ (Refs. 2 and 3) and RMn_2O_5 (Ref. 6) (*R* =rare earths) points to the important role of magnetic frustration in enhancing the ME coupling. An enhanced magnetodielectric effect (45% at 9 T) has also been observed in La-doped $BiMnO_3$.[8] Yang *et al.*[8] showed that the magnetodielectric effect in this system is dynamically enhanced due to the magnetic field control of the dielectric relaxation.

Multifunctional double perovskite oxides of $La_2BB'O_6$ (*B*=transition metal such as Ni and Co; *B'*=Mn) composition recently gained much interest both because of their rich physics and their prospects for technological applications.[9–12] Depending on the relative size and oxidation state, the *B* and *B'* ions can be crystallographically completely ordered, making up a rocksalt-type lattice. Large magnetic-field-induced changes in the resistivity and dielectric properties have been observed in both bulk polycrystalline samples and epitaxial thin films of the ordered double perovskite LNMO.[9,12]

The magnetic properties of bulk LNMO have been widely studied over the years in order to gain better understanding of the nature of the magnetic exchange interactions in this compound.[9,13–21] It was suggested that LNMO is a ferromagnetic semiconductor with ordered Ni and Mn ions, compared to the antiferromagnetic and paramagnetic behaviors of

$LaMnO_3$ and $LaNiO_3$, respectively. Goodenough *et al.*[13] initially attributed ferromagnetism in LNMO to Mn^{3+}-O-Ni^{3+} superexchange interactions, where low-spin Ni^{3+} and high-spin Mn^{3+} are both Jahn-Teller ions. On the other hand, Blasse[14] argued that ferromagnetism is entirely due to the Mn^{4+}-O-Ni^{2+} superexchange interactions, which is supported by ^{55}Mn NMR (Refs. 15 and 16) and neutron diffraction studies.[20] Joseph Joly *et al.*[18] more recently showed the existence of two different spin states of Mn and Ni in bulk LNMO samples synthesized at different temperatures, and charge disproportionation of the Mn^{4+}-$Ni^{2+} \rightarrow Mn^{3+}$-$Ni^{3+}$ type occurs when the low-temperature synthesized LNMO is annealed at high temperatures. $LaMnO_3$ has an orthorhombic perovskite structure, whereas $LaNiO_3$ is rhombohedral. Because of the different structures of the end members, it is likely that LNMO is polymorphic with two different structures. Indeed, the structure of LNMO is found to be rhombohedral ($R\bar{3}$) at high temperatures and it transforms to an orthorhombic (*Pbnm*, with *c* being the long axis) or a monoclinic structure at low temperatures. These two structures typically coexist at room temperature.[19–21] In contrast to earlier x-ray diffraction results, neutron diffraction data indicate a reduction from the orthorhombic symmetry to the monoclinic subgroup $P2_1/n$ due to the *B* cation ordering.[9,19]

The oxygen anion plays a critical role in dictating the physical properties of the manganites. Being at the center of the *B*-O-*B* bond, its presence or absence can greatly influence the valence states, local lattice distortions, as well as the orbital order. In previous works, we reported on the epitaxial growth of LNMO thin films on different substrates at an 800 mTorr oxygen. The films were crystallized in the monoclinic (orthorhombic) structure and they exhibited excellent magnetic properties.[12,22] In the present study, we have investigated in detail the influence of oxygen deficiency and other defects on the structural and magnetic properties of LNMO thin films deposited on various substrates by varying the oxygen background pressure during growth. The effect of reducing the film thickness on its structural and magnetic properties has also been studied.

II. EXPERIMENT

The LNMO thin films were deposited on $SrTiO_3$ (STO) (cubic, 001), $NdGaO_3$ (NGO) [orthorhombic, with (110) orientation], $LaAlO_3$ (LAO) (cubic, 001), and MgO (cubic, 001) substrates by the pulsed laser deposition (PLD) technique by using a sintered, stoichiometric, and monophasic LNMO target.[22] The substrate temperature, target-substrate distance, laser fluence, and repetition frequency were held constant for all the deposited samples. The films were grown at different background oxygen pressures (25–800 mTorr) while maintaining the substrate temperature at 750 °C. The target-to-substrate distance was fixed at 45 mm for all the deposition runs. A KrF excimer laser (248 nm), with a repetition rate of 2 Hz, was used for ablation with an energy density of about 1.5 J/cm^2 at the target. Films in the thickness range of 10–350 nm (as determined by using low-angle x-ray reflectometry) were deposited by controlling the number of laser pulses used for deposition. After deposition, the films were annealed *in situ* for 1 h in a 760 Torr oxygen and then slowly cooled down to room temperature at 15 °C/min. Details regarding the structural quality and lattice parameters of the films were obtained by using a Philips X'Pert x-ray diffractometer. The chemical composition and thickness of the LNMO thin films were determined by using the Rutherford backscattering spectrometry (RBS) and energy dispersive x-ray analysis (EDX).

Electron microscopy observations were carried out in an aberration corrected scanning transmission electron microscope (STEM) (VG Microscopes HB501UX) operated at 100 keV equipped with a Nion aberration corrector and a Gatan Enfina electron energy loss spectrometer (EELS), and in an aberration corrected transmission electron microscope (TEM) (FEI Titan) at 300 kV. Specimens for the STEM analysis were prepared by conventional methods, grinding, dimpling, and Ar ion milling. Details regarding the oxidation states were obtained from the analysis of the EELS data of the O *K* edge around 530 eV and the Mn *L* edge around 644 eV.

The Raman spectra of the films were examined in the backscattering geometry by using a Jobin–Yvon LabRam-IR micro-Raman spectrometer. A 632.8 nm He-Ne laser was used for excitation. Additionally, polarized Raman measurements were carried out on some of the samples with 488 nm Ar^+ excitation by using a HR640 single spectrometer equipped with a microscope and a liquid nitrogen cooled charge coupled device detector. X-ray photoemission spectroscopy (XPS) was carried out by using an Mg $K\alpha$ source ($h\nu$=1253.6 eV). To remove surface contaminants before the XPS analysis, the films were gently sputter cleaned for 30 s with Ar^+ ions at 4 kV. A superconducting quantum interference device magnetometer (MPMS, Quantum Design) was used to measure the temperature-dependent magnetization properties. Magnetic hysteresis loops for the LNMO films at different temperatures were obtained by using a vibrating sample magnetometer (Oxford).

III. RESULTS AND DISCUSSION

A. Structural properties

Previous XRD θ-2θ studies for LNMO films grown on STO, NGO, LAO, and MgO substrates have shown that the films are single phased, exhibiting a strong preferential orientation.[22] Φ scans, which were recorded around the (103) reflections of the LNMO thin film pseudocubic subcell and the corresponding (103) reflections from the STO and NGO substrates obtained by in-plane rotation of the samples, exhibit four peaks separated by 90° from each other, revealing a fourfold symmetry. Additionally, the angular positions of the peaks from the LNMO thin film are separated by 45° and 0° with respect to those of the STO and NGO substrates, respectively. The appearance of peaks at the 45° separation suggests a 45° rotation of the LNMO thin film in the plane of the STO substrate. From the Φ-scan measurements, we infer that the epitaxial relationships for the LNMO thin films grown on the STO and NGO substrates are (002) LNMO$\|$(001) STO and [$\bar{1}$10] LNMO$\|$[100] STO; (110)

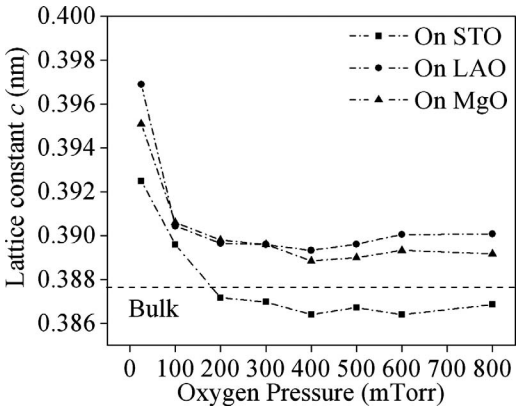

FIG. 1. Plot of the *c*-axis lattice parameter of LNMO thin films grown on STO, LAO, and MgO substrates versus oxygen background pressure during growth.

LNMO∥(110) NGO and [001] LNMO∥[001] NGO.

Variations in the *c* lattice parameter of LNMO thin films on STO, LAO, and MgO as a function of oxygen pressure are plotted in Fig. 1. The squares, circles, and triangles represent the experimental data points, and the dash-dot lines are provided as a guide to the eye. The films grown at low oxygen pressures exhibit an expanded *c* lattice parameter as compared to the pseudocubic bulk value (0.3876 nm, Ref. 19). With increasing oxygen pressure, the *c* lattice parameter steadily decreases before leveling off at higher pressures, as seen in Fig. 1.

The growth of the thin films under different oxygen background pressures can result in variations in the defect concentration from two major sources: (i) oxygen vacancies and (ii) the varying energy and flux of the species impinging upon the surface of the growing film. Park and Chadi[23] investigated the nature of the atomic relaxations around oxygen-vacancy defects in the ferroelectric perovskite $PbTiO_3$ through first-principles pseudopotential total energy calculations. The oxygen vacancies are considered to be double donor defects. When oxygen vacancies exist in the sample, the nearest two Ti and four Pb cations of 2+ effective charge corresponding to the oxygen vacancy are displaced away, while the eight next closest O anions are attracted toward the defect. As a consequence, the lattice parameter of $PbTiO_3$ decreases. On the other hand, Maria *et al.*[24] argued that the growth conditions during pulsed laser deposition of the perovskite oxide $SrRuO_3$ when operating at low background pressures favor bombardment from high energy species. This results in the growth of films with expanded lattice constants caused by defects other than oxygen vacancies.

In an attempt to determine which factor has the greatest influence on the growth of LNMO, we have deposited LNMO films by using a 50 mTorr gas mixture of Ar/O_2 with a ratio of 10:1. One would expect that the oxygen-vacancy concentration in the film grown under the 50 mTorr Ar/O_2 mixed gas atmosphere would be higher than that under a 50 mTorr of pure O_2. However, at the same time, due to the similarities in the scattering cross sections of Ar and O_2, the bombardment from high energy species experienced by the films during growth is expected to be similar in both cases. The XRD θ-2θ scan of the LNMO (004) diffraction peak positions are essentially identical for the two films (not shown). This suggests that while the creation of oxygen defects, which influences the structural parameters of the LNMO thin films, is important at low oxygen pressures, the decrease in the lattice parameter observed at higher background pressures ($\geq$5 mTorr) primarily results from a decrease in the defect concentration because of reduction in the bombardment of high energy species on the surface of the growing film.

The chemical composition and stoichiometry of the LNMO films grown at 25, 200, and 800 mTorr O_2 have been analyzed by RBS, and the results are shown in Table I. All the LNMO films appear oxygen deficient with respect to the stoichiometric composition. It should, however, be noted that the error in determining the O content is significantly larger than for the other elements due to the presence of the relatively large O background signal from the substrate. Nonetheless, at higher oxygen pressures, the oxygen-to-metal ratio increases and the Ni/Mn ratio approaches 1:1, indicating that the films are closer to the bulk stoichiometry. The presence of excess La (with respect to Ni+Mn) is also indicated for the film grown at a low pressure (25 mTorr) and it becomes close to stoichiometric at higher pressures. The presence of some excess La in the films grown at low oxygen pressures was also confirmed from chemical composition analysis by using EDX. While all the films grown in a 100 mTorr O_2 and higher pressures showed a La:Mn:Ni stoichiometry of close to 2:1:1 to within $\pm$5%, those grown at lower pressures showed some deviation. For example, a film grown with a 0.1 mTorr O_2 provided a La:Ni:Mn ratio of 2.16:0.96:1.00 from the EDX analysis.

TABLE I. The chemical composition and stoichiometry ratio of LNMO thin films grown on STO substrates under various oxygen pressures as determined from RBS measurements.

Oxygen pressure (mTorr)	Chemical composition					
	La (at. %)	Ni (at. %)	Mn (at. %)	O (at. %)	La:Ni:Mn	O: (La+Ni+Mn)
25	23.4 ± 1.0	11.0 ± 2.0	9.8 ± 2.0	55.8 ± 5.0	2.39: 1.12: 1	1.26
200	21.1 ± 1.0	11.4 ± 2.0	10.3 ± 2.0	57.2 ± 5.0	2.05: 1.11: 1	1.34
800	20.6 ± 1.0	11.3 ± 2.0	10.8 ± 2.0	57.3 ± 5.0	1.91: 1.04: 1	1.34

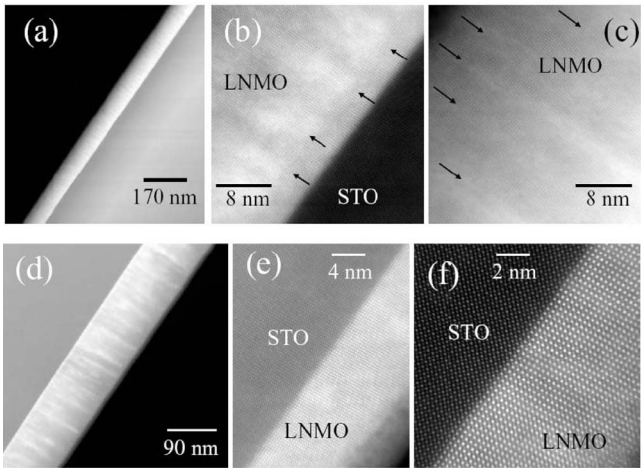

FIG. 2. Low-magnification cross-section STEM images of LNMO films on STO substrate grown under (a) 100 mTorr and (d) 800 mTorr O_2. High-resolution STEM images near the interface region showing the epitaxial growth of LNMO films on STO substrates grown under (b) 100 mTorr and (e) 800 mTorr O_2. High-resolution STEM images of LNMO films grown under (c) 100 mTorr and (f) 800 mTorr O_2.

B. Scanning transmission electron microscopy, transmission electron microscopy, and electron energy loss spectroscopy analyses

Figures 2(a) and 2(d) show the low-magnification cross-section STEM images of the LNMO thin films grown on the STO substrates under 100 and 800 mTorr O_2, respectively. The films appear flat and homogeneous over large lateral distances. There are regions of accumulated strain in the samples (these are the areas of brighter contrast, showing bright halos) probably due to some degree of lattice mismatch between the film and substrate. They could also result from the presence of oxygen vacancies or other defects. The contrast resulting from strain appears more likely because the halos arise at the interface and propagate through the sample surface. The epitaxial growth of the film on STO is confirmed by the high-resolution STEM images. The excellent unit-cell to unit-cell epitaxial relationship between the LNMO films and STO substrates can be seen in Figs. 2(b)–2(f). The films are confirmed to grow epitaxially and the interface between the LNMO thin films and the STO substrate is sharp and coherent. There is no evidence of secondary phases or any chemical reaction in the interface region over large distances.

It is worth noting that for the film grown under 100 mTorr O_2 there is a layer of about 5 nm near the interface that essentially appears defect-free. This most likely implies that at the initial stage of epitaxial growth, the LNMO film is strained to match its lattice parameter with that of the STO substrate. When the film reaches a critical thickness, defects form in the LNMO film as a result of strain relaxation. Subsequently, defects are generated that extend all the way through the sample [Fig. 2(c)] until they reach the surface (as shown by the arrows in the figure). On the other hand, for the film grown at 800 mTorr O_2, the structural quality is extremely high, being free of any major defects throughout the cross section of the film. Thus, a higher O_2 background concentration appears to have a significant influence in improving the structural quality of the LNMO film.

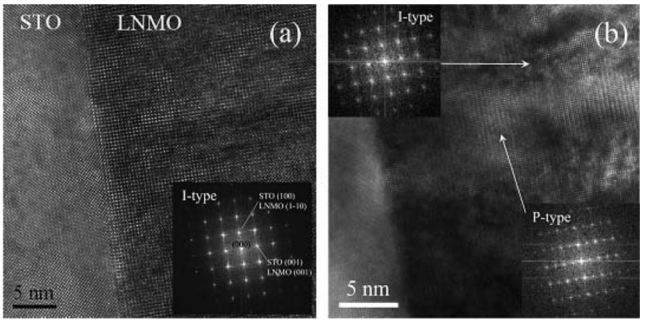

FIG. 3. Phase contrast high-resolution TEM images of LNMO films on STO substrate under (a) 100 mTorr and (b) 800 mTorr O_2. The insets show the FFT of (a) the whole image and (b) the areas indicated with arrows.

Phase contrast high-resolution TEM (HRTEM) images of the LNMO thin films grown on STO under 100 and 800 mTorr O_2 are displayed in Figs. 3(a) and 3(b), respectively. In agreement with the STEM results, the 100 mTorr O_2 sample shows a strained, defect-free LNMO layer in the early stages of growth. At a thickness of $\sim 5-10$ nm, the strain in the film is relaxed, nucleating numerous defects in the remaining thickness of the film, as seen in Fig. 3(a). The low oxygen pressure LNMO layer is structurally essentially single phase. The fast fourier transform (FFT) shown in the inset of Fig. 3(a) corresponds to the same centered structure observed by Singh *et al.*[25] with lattice parameters $a \cong b \cong 5.5$ Å and $c \cong 7.8$ Å, which is labeled as *I* type. Symmetry considerations suggest that a long-range cationic ordering is not compatible with this structure and may thus provide evidence for antisite defects.[25] On the other hand, HRTEM images of the 800 mTorr O_2 film show that this sample is structurally biphasic at room temperature, as seen in Fig. 3(b). In addition to the same *I*-type crystal structure observed in the low oxygen pressure film, numerous regions of the layer crystallize in a second structure characterized by a new set of reflections with even *l* index. This phase was also observed by Singh *et al.* and labeled as "*P* type" due to the breaking of the centered symmetry of the *I* phase. The appearance of Moiré fringes is evidence of the superposition of *I*- and *P*-type nanodomains. The biphasic nature of the film is consistent with bulk results, which show the presence of both the rhombohedral and monoclinic phases coexisting over a wide temperature range, including at room temperature. Even though these results are inconclusive, the appearance of a new set of reflections forbidden for centered orthorhombic (monoclinic) structures indicates a symmetry reduction that might point to Ni/Mn ordering.[25] Thorough TEM and electron diffraction studies along the different zone axes would be required to clarify this point.

The analysis of the EELS images of the prepeak of the O *K* edge, which were averaged over 360 points (covering a lateral area of 90×140 nm^2), shows an average oxidation state of the transition metal ions (combination of Mn and Ni) of 2.94 ± 0.18 and 3.09 ± 0.04 for the samples grown under

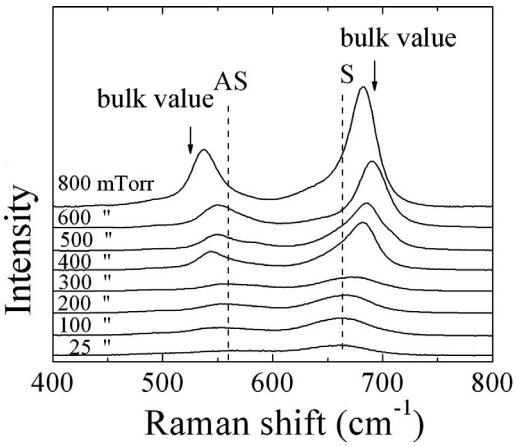

FIG. 4. Raman spectra of LNMO films grown on (001) LAO substrates under different oxygen pressure conditions.

100 and 800 mTorr O_2, respectively. This is consistent with an average oxidation state of +3 for M in the $LaMO_3$ formula unit. For quantification purposes, the O *K* edges from $LaMnO_3$ and $CaMnO_3$ have been used as a reference.

The analysis of the Mn *L* edge under the same conditions shows an oxidation state of 3.52 ± 0.55 and 3.98 ± 0.10 for the samples grown under 100 and 800 mTorr, respectively. So it appears that there could be a mixed valence Mn^{3+}/Mn^{4+} in the system, and increasing charge disproportionation of the type Mn^{4+}-$Ni^{2+} \rightarrow Mn^{3+}$-$Ni^{3+}$ occurs with decreasing oxygen pressure. Although the error bars are too large to draw this conclusion from the EELS result alone, this is confirmed by the Raman and XPS results, which will be presented below. A large deviation in the oxidation values is observed in the sample grown under 100 mTorr from pixel to pixel, suggesting that the sample may be electronically inhomogeneous due to the presence of oxygen and other types of defects in the film.

C. Raman spectra

Useful information about the crystal symmetry, internal stress, cation disorder, local lattice distortion, oxygen deficiency, and presence of impurity phases can be obtained by using Raman spectroscopy.[26–30] Figure 4 shows the unpolarized Raman spectra of the LNMO thin films (632.8 nm excitation) grown on (001)-oriented LAO substrates under different oxygen pressures. For clarity, the Raman spectra are displayed with upward base line shifts as the oxygen pressure increases from 25 to 800 mTorr. The spectra are dominated by two broad peaks at ~540 and ~685 cm^{-1}. Previously, these two peaks had been tentatively assigned to the antisymmetric stretching (AS) and symmetric stretching (S) vibrations of BO_6 octahedra, respectively, of the orthorhombic *Pbnm* (or *Pnma*) structure.[22,26] Recent Raman studies of the polarized Raman spectra have confirmed the AS and S characters of these modes but within the monoclinic ($P2_1/n$) or rhombohedral ($R\bar{3}$) structures, which, unlike *Pnma*, can accommodate ordering of the Ni and Mn ions.[28]

It can be observed from Fig. 4 that the AS mode in the LNMO thin films, in general, occurs at a higher frequency

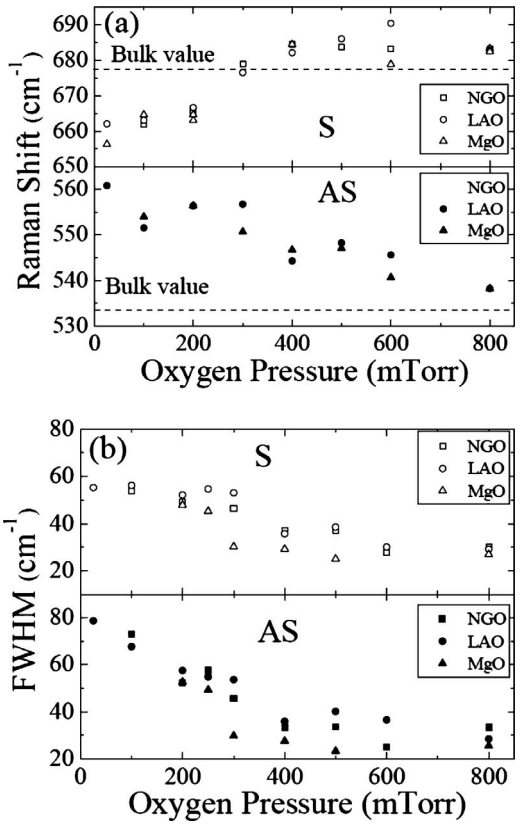

FIG. 5. Oxygen pressure dependence of (a) the Raman shift and (b) the peak width for the AS and S stretching modes.

(blueshift) than the corresponding mode in the bulk, while the S mode appears at a lower frequency (redshift) than the LNMO bulk value.[27] Moreover, the spectra show that the blue- and redshift of the Raman modes increase for films deposited at low oxygen pressures. Simultaneously, the peak intensity decreases and the width of the peaks broaden. The evolution of the peak frequencies and widths (full width at half maximum) with oxygen pressure is illustrated in more detail in Fig. 5. The shift of the AS and S modes in opposite directions is likely related to the fact that the AS mode in the $P2_1/n$ structure primarily involves in-plane antisymmetric stretching vibrations, whereas the S mode is fully symmetric and involves both the in-plane and out-of-plane stretching vibrations of the NiO_6 and MnO_6 octahedra. The increase in the out-of-plane lattice parameter in response to the decreasing oxygen pressure, which is discussed in the previous section, will result in a decrease in only the S mode frequency.

The observed broadening and intensity decrease of the Raman spectral structures with decrease in the oxygen pressure has a reasonable explanation in larger lattice distortions with increasing oxygen deficiency, incomplete ordering at *B* and *B′* sites, and coexistence of non-Jahn-Teller (Ni^{2+}, Mn^{4+}) and Jahn-Teller (Ni^{3+}, Mn^{3+}) ions. These effects were recently discussed in the case of mixed valence manganites by Iliev *et al.*[30] and can be summarized as follows. At relatively low concentrations, the local distortions act as scattering centers for phonons, thus shortening the phonon lifetimes and broadening the Raman lines corresponding to zone-center normal modes. The stronger distortions in the oxygen sublat-

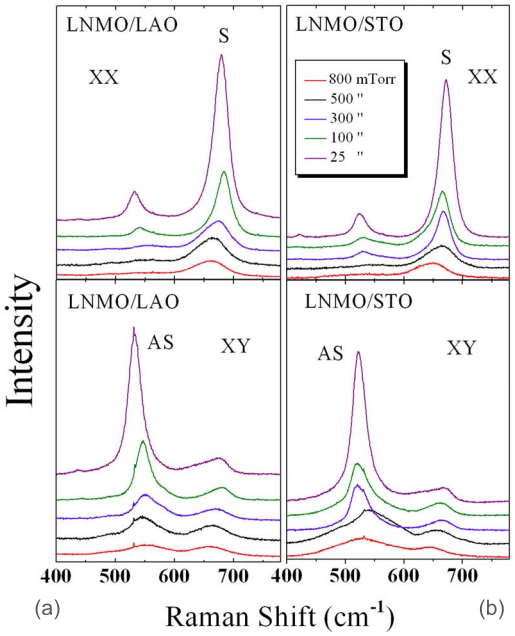

FIG. 6. (Color online) Polarized Raman spectra in the *xx* and *xy* scattering configurations for LNMO films deposited on (a) LAO and (b) STO substrates under different oxygen pressure conditions.

tice as a whole result in breakdown of translation symmetry and phonons from the whole Brillouin zone can contribute to the scattering. This gives rise to broad bands, reflecting the "smeared" one phonon density of states, which has maxima at frequencies corresponding to those of zone boundary phonons.

In order to assess the relative contribution of incomplete *B*-site ordering versus other types of defects formed at low oxygen concentrations, we have performed polarized Raman measurements (488 nm excitation) on some of the films grown on LAO and STO substrates as a function of the oxygen pressure. The spectra were taken with exact xx, $x'x'$, yy, xy, and $x'y'$ scattering configurations, where $x\|[100]$, $x'\|[110]$, $y\|[010]$, $y'\|[\bar{1}10]$ (with the first and second letters referring to the polarization direction of the incident and the scattered light, respectively). The spectra for the xx and xy scattering configurations are shown in Fig. 6. The evolution of the peak frequencies and width with oxygen pressure is similar to that observed in Fig. 4 for the 632.8 nm excitation with no polarization. In addition, information regarding the changes in the ordering at *B* and *B'* can be obtained from the polarization measurements. The *B*-site ordered and disordered structures belong to different symmetry groups and the corresponding Raman spectra, if taken in exact scattering configurations, obey different Raman polarization selection rules. In the ordered structures ($P2_1/n$ or $R\bar{3}$) the S Raman mode between 650 and 700 cm^{-1} is allowed in parallel (xx or yy) but forbidden with crossed xy scattering configuration.[28] On the other hand, the AS mode between 500 and 550 cm^{-1} is allowed in xy but forbidden with the xx/yy configuration. The fully disordered structure belongs to the *Pbnm* space group, where the polarization selection rules are just the opposite. The S mode should be present in the cross polarized

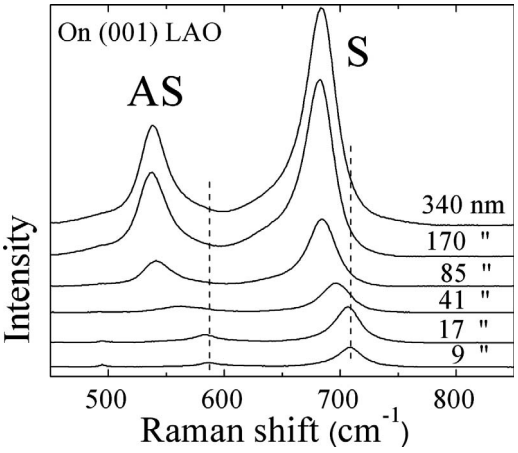

FIG. 7. Raman spectra of LNMO films of different thicknesses grown on (001) LAO substrates.

XY spectra, and the AS mode in the xx/yy spectra.

As seen in Fig. 6, all spectra exhibit a much stronger S peak with xx polarization, whereas the AS peak is stronger with xy polarization. This is clear evidence that for all oxygen pressures, the structure is dominantly ordered over the short length scale probed by Raman. At the same time, the AS and S are much broader for the films obtained at the 25 and 100 mTorr pressures. Given that the AS and S mainly involve oxygen vibrations, this broadening has to be primarily related to disorder of the oxygen sublattice. Other than the partial *B*-site disorder, the broadening is governed by nonstoichiometry, the coexistence of Mn^{3+}, Mn^{4+}, Ni^{2+}, and Ni^{3+}, which creates static or dynamical Jahn-Teller disorder, etc.

Figure 7 shows the Raman spectra of LNMO films of different thicknesses grown under the same background O_2 pressure (800 mTorr) excited by using the unpolarized 632.8 nm light source. The decrease in peak intensity with reduction in film thickness is in a large part due to the reduced scattering volume. The frequencies of the AS and S modes of the thinner films are appreciably higher than the corresponding phonon frequencies in bulk LNMO.[26,27] This is shown in more detail in Fig. 8. The blueshifts are related to compressive stress in the LNMO thin films, resulting both from the lattice mismatch between the film and the substrate

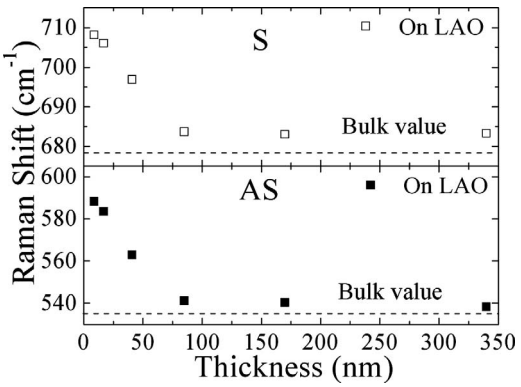

FIG. 8. Raman shifts for the AS and S modes as a function of film thickness.

and the thermal expansion coefficient difference. These two factors are considered for LNMO thin films as follows. First, due to the lattice mismatch, the compressive strain is relaxed with increasing film thickness, and it will be fully relaxed when the film thickness exceeds a critical thickness. From Fig. 8, one finds that there is no further shift of the peaks when the film thickness exceeds 85 nm, indicating that the critical thickness is between 40 and 80 nm. Second, when a LNMO film is cooled from the deposition temperature (750 °C) to room temperature, both the film and the substrate are contracted due to the thermal expansion effect. Because of differences in the thermal expansion coefficients, there will be a stress generated because of the differential contraction. However, the lattice of the LNMO film cannot be contracted according to its thermal expansion due to the strong clamping effect of the substrate. It is therefore reasonable to assume that the LNMO films will contract according to the thermal expansion behavior of the LAO substrate. Hence, a strain is imposed on the LNMO thin film, which is also confirmed from the STEM and TEM measurements (see Figs. 2 and 3).

D. X-ray photoemission spectroscopy measurements

XPS measurements have been carried out in order to obtain more detailed information about the electronic structure of the LNMO thin films. The valence band (VB) and corresponding core-level spectra of Mn $2p$, Ni $2p$, and O $1s$ of the LNMO films grown on a STO substrate grown under 200 and 800 mTorr O_2 are shown in Fig. 9(a). The VB displays the characteristic triple-peak structure located at 5.86, 4.75, and 2.85 eV, respectively. The former two peaks can be primarily attributed to the Mn $3d-O\ 2p$ and Ni $3d-O\ 2p$ bonding states, while the latter is mainly associated with O $2p$ nonbonding states.[31,32] The entire VB region exhibits the characteristics of extensively hybridized Mn $3d-O\ 2p$ and Ni $3d-O\ 2p$ orbitals.

The $2p$ core-level XPS spectra of Mn in the LNMO thin films grown at 200 and 800 mTorr are shown in Fig. 9(b). The binding energy (BE) of the $2p_{3/2}$ peak is 641.21 and 641.52 eV, respectively, for the two samples. There is a general trend that the core-level binding energy increases with increasing the oxidation state of a given ion, provided that the ions are located in similar coordination environments. Therefore, the difference between the BEs of Mn $2p_{3/2}$ for these two samples indicates that the oxidation state of Mn in the sample grown under the 800 mTorr oxygen is higher than that of the one grown under 200 mTorr. This is consistent with the results from Raman scattering and EELS measurements, suggesting that charge disproportionation of the Mn^{4+}-$Ni^{2+} \rightarrow Mn^{3+}$-$Ni^{3+}$ type likely occurs with decreasing oxygen pressure during film growth.

Figure 9(c) shows the $2p$ core-level XPS spectra of Ni in the samples grown at 200 and 800 mTorr. Coincidentally, the binding energy of the satellite peak of La $3d_{3/2}$ is almost identical to the BE of $2p_{3/2}$ of Ni in oxides, and therefore, these peaks overlap for compounds containing both La and Ni. The BE of Ni $2p_{3/2}$ in the sample grown at 800 mTorr is found to be somewhat larger than that for the one grown at

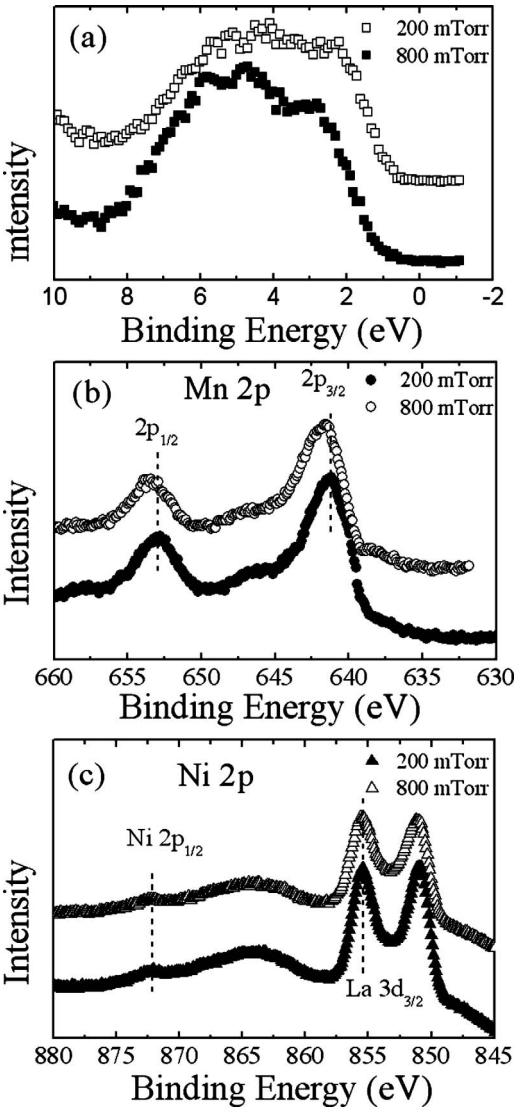

FIG. 9. XPS measurement of the LNMO thin films grown under 200 and 800 mTorr O_2: (a) valence band spectra, (b) Mn $2p$ XPS spectra, and (c) Ni $2p$ XPS spectra.

200 mTorr (855.53 and 855.46 eV for the samples at 800 and 200 mTorr, respectively). A similar difference in the BE is observed for the Ni $2p_{1/2}$ for the two samples. The observation that the core-level BE increases with increasing oxidation state of a given ion breaks down when the number of unpaired electrons changes due to a change in the spin state of a given ion. It was previously reported that the Ni $2p_{3/2}$ BE of Ni_2O_3 containing low-spin Ni^{3+} is lower than that of NiO containing Ni^{2+}.[33] The lower BE of Ni $2p_{3/2}$ for the sample at 200 mTorr indicates that the oxidation state of Ni in the sample at 800 mTorr is lower than that at 200 mTorr. The spin states of Ni in the two samples are in accordance with the spin states of Mn, which adjusts to ensure charge neutrality and oxygen stoichiometry.

E. Magnetic properties

The magnetization as a function of temperature of the LNMO films grown on LAO substrates was measured in

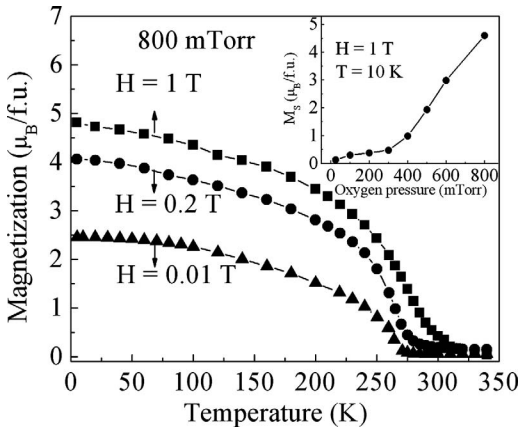

FIG. 10. Temperature dependence of the magnetization for LNMO film grown under 800 mTorr O_2 measured in 0.01, 0.2, and 1 T magnetic fields. The inset shows a plot of the saturation magnetization in a 1 T magnetic field at 10 K of LNMO thin films versus the oxygen pressure during growth.

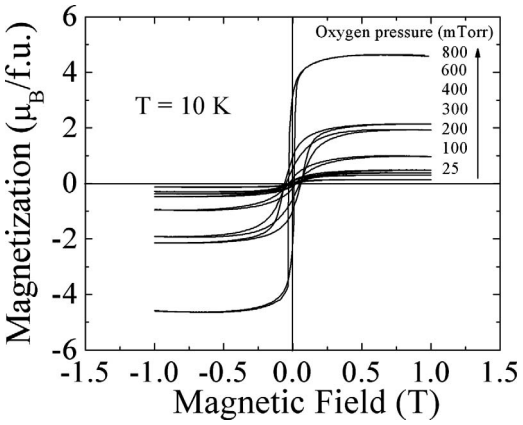

FIG. 11. $M(H)$ hysteresis loops for the LNMO films grown under different oxygen pressures on LAO substrates measured at 10 K.

different magnetic fields (0.01–1 T). Before the measurement, the samples are heated to a temperature of 330 K to eliminate any prior magnetic history. The temperature dependence of the magnetization of a film grown under 800 mTorr O_2, which is measured under applied magnetic fields of 0.01, 0.2, and 1 T, is shown in Fig. 10. We have determined the ferromagnetic Curie temperatures T_C of films grown at different oxygen pressure by taking the derivative of the magnetization with respect to temperature (dM/dT) in a magnetic field of 0.01 T. The results are summarized in Table II. Additionally, we have determined the T_C for some of the samples by using the Arrott plot method from the M versus H measurements near the transition temperature (plots of M^2 vs H/M that are extrapolated to zero field).[34] This method yielded T_C values to within ±5 K of those listed in Table II.

Figure 11 shows the magnetic hysteresis loops measured at 10 K over the field range $-1\ \mathrm{T} \leqslant H \leqslant 1\ \mathrm{T}$ for films grown at different oxygen pressures. They provide the saturation magnetization M_s (10 K, 1 T), coercivity H_c (10 K), and remanence M_r (10 K) data, which are listed in Table II. While a broadening of the ferromagnetic-paramagnetic transition is observed, the T_C essentially remains unchanged (270–290 K) for the films grown under different oxygen pressures. However, both M_s and M_r steadily increase with increasing oxygen pressure, while H_c does not show any systematic variation. The inset in Fig. 10 summarizes the saturation moment as a function of oxygen pressure. It is clear that the saturation moment increases with increasing oxygen pressure, and the highest saturation moment is obtained for the film grown at 800 mTorr, which is closest to being stoichiometric in oxygen and has a $T_C \approx 275$ K. It exhibits a saturation magnetization (M_s) at 10 K in 1 T field of $4.63\mu_B$/f.u., which approaches the theoretical spin-only value of $5\mu_B$/f.u. for fully ordered $La_2Ni^{2+}Mn^{4+}O_6$. The lower than expected moment in the low-pressure grown films may be explained by the increased structural distortions involving the BO_6 octahedra as well as other interatomic structural features, such as bond angles, bond length, and the disorder of B-site ions caused by the increase in the concentration of Mn^{3+} and Ni^{3+} ions and oxygen vacancies.

Since stoichiometric La_2NiMnO_6 is a semiconductor,[10] double exchange is not expected to be a contributing factor, and the magnetic properties can be interpreted based on the rules for the sign of the spin-spin superexchange interac-

TABLE II. The magnetic properties of LNMO thin films on LAO substrates grown under different oxygen pressures. F refers to ferromagnetism and T_C is the Curie temperature. M_s (10 K, 1 T), M_r, and H_c are the magnetization in a 1 T magnetic field, the remanent magnetization, and the coercivity at 10 K, respectively.

Oxygen pressure (mTorr)	Type of magnetic behavior	Magnetic transition temperature (K)	M_s (10 K, 1 T) (μ_B/f.u)	M_r (10 K) (μ_B/f.u)	H_c (10 K) (Oe)
25	*F*	270	0.14	0.09	233
100	*F*	271	0.30	0.09	295
200	*F*	270	0.38	0.06	162
300	*F*	280	0.48	0.10	291
400	*F*	283	0.99	0.17	239
500	*F*	290	1.93	0.54	495
600	*F*	289	2.98	0.97	586
800	*F*	275	4.63	2.70	152

tions: (1) ferromagnetic (FM) coupling in the case of half-filled to empty orbital virtual spin transfer, as in e^0-O-e^2, such as $Mn^{4+}(e^0)$-O-$Ni^{2+}(e^2)$; (2) antiferromagnetic (AFM) coupling in the case of half-filled to half-filled orbital virtual change transfer, as in e^2-O-e^2 or t^3-O-t^3, such as $Ni^{2+}(e^2)$-O-$Ni^{2+}(e^2)$ and $Mn^{4+}(t^3)$-O-$Mn^{4+}(t^3)$. In addition, (3) interactions via σ-bonding e orbital dominate those by π-bonding t orbitals where both are present in the same total interaction. and (4) Jahn-Teller ions have a single electron in twofold-degenerate fluctuating e-orbital occupation as in e^1-O-e^1 [$Ni^{3+}(e^1)$-O-$Mn^{3+}(e^1)$, $Mn^{3+}(e^1)$-O-$Mn^{3+}(e^1)$, and $Ni^{3+}(e^1)$-O-$Ni^{3+}(e^1)$], giving a three-dimensional FM, vibronic superexchange interaction.[11,21] From our experimental data, the LNMO samples grown under different oxygen pressures appear to contain varying fractions of Mn^{4+}, Mn^{3+}, Ni^{2+}, and Ni^{3+} ions. The FM exchange interactions are Mn^{4+}-O-Ni^{2+}, Mn^{3+}-O-Ni^{3+}, Ni^{3+}-O-Ni^{3+}, Mn^{3+}-O-Mn^{3+}, and Mn^{3+}-O-Mn^{4+}. The AFM superexchange interactions are Mn^{4+}-O-Mn^{4+}, Ni^{2+}-O-Mn^{3+} and Ni^{2+}-O-Ni^{2+}. In the samples grown under high oxygen pressures, ordering of Mn^{4+} and Ni^{2+} ions in $La_2Ni^{2+}Mn^{4+}O_6$ leads to long-range FM Mn^{4+}-O-Ni^{2+} (e^0-O-e^2) superexchange interactions, but point disorder can create AFM Mn^{4+}-O-Mn^{4+} or Ni^{2+}-O-Ni^{2+} interactions with the antisite ions.[26] Moreover, in an ordered double perovskite, nucleation of atomic order at different positions results in antiphase boundaries if the positions of the Ni^{2+} and Mn^{4+} are inverted. The antiphase interface between the two regions would have AFM Ni^{2+}-O-Ni^{2+} or Mn^{4+}-O-Mn^{4+} interactions, whereas both ordered regions would have FM Ni^{2+}-O-Mn^{4+} interactions. Oxygen vacancies induce transfer of an electron from the e band of Ni^{2+} ions to neighboring Mn^{4+} ions, creating Ni^{3+} and Mn^{3+} Jahn-Teller ions, which cause local Jahn-Teller distortions of the octahedral sites. The Jahn-Teller distortions would inhibit long-range ordering of Ni and Mn on different lattice sites, stabilizing vibronic FM Mn^{3+}-O-Mn^{3+}, Ni^{3+}-O-Mn^{3+}, and Ni^{3+}-O-Ni^{3+} superexchange interactions in an atomically disordered volume. As pointed by Dass and Goodenough,[11] such a vibronic superexchange gives a small stabilization as compared to the static FM Mn^{4+}-O-Ni^{2+} superexchange, thus, the magnetization is decreased. On the other hand, Poeppelmeier *et al.*[35,36] showed that oxygen vacancies can lead to reversal of the sign of the spin-spin superexchange interactions. In the case of $CaMnO_3$ samples, both the Mn^{3+}-O-Mn^{3+} and Mn^{4+}-O-Mn^{3+} superexchange interactions are positive in the orbitally disordered phase if manganese ions are surrounded by six oxygen anions. However, these interactions become AFM in the case of fivefold coordination of the manganese ions. Therefore, decrease in oxygen content leads to increasing amount of B-site ions with a fivefold coordination and destroys the long-range FM order. This induces the AFM part of the superexchange interactions to be enhanced, which accounts for the reduced magnetization in the samples grown under lower oxygen pressures.

In order to investigate the effect of epitaxial strain on the magnetic properties, we have measured the magnetization of LNMO films of different thicknesses, which were all grown with a background pressure of 800 mTorr O_2. Hysteresis loops measured at 10 K after zero-field cooling are shown in Fig. 12. All the samples display hysteresis curves with close

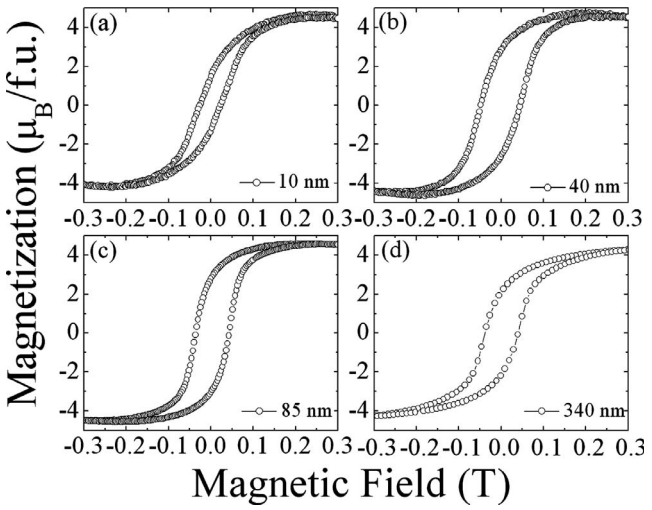

FIG. 12. $M(H)$ hysteresis loops for LNMO films grown on LAO substrates under 800 mTorr O_2 at 10 K with film thicknesses of (a) 10 nm, (b) 40 nm, (c) 85 nm, and (d) 340 nm.

to a rectangular shape, with a high remanence and a low coercive field. The coercive field of the samples is in the range of 300–500 Oe, and they all display similar values of the saturation magnetization of about $4.5\mu_B$/f.u. The critical thickness for strain relaxation in the films is about 40–80 nm, as determined from the Raman spectra. However, even when the film thickness is larger than the critical thickness, some lattice distortion can still persist. The extent of lattice distortion and inhomogeneities in the LNMO thin films decreases the degree of ferromagnetic long-range order, leading to a decreased magnetization. Since the films of different thicknesses exhibit the same saturation magnetization, the strain effect on the magnetic properties appears to be quite small. This suggests that the magnetostrictive effect and, correspondingly, the direct magnetoelectric coupling in this system may be relatively weak.

IV. CONCLUSION

In summary, LNMO thin films have been grown on various substrates over a wide oxygen pressure range by using PLD. The oxygen environment during growth has a pronounced effect on the crystal structure, chemical composition, and magnetic properties of the films. The XRD and RBS results indicate that with decreasing oxygen pressure during deposition, the oxygen deficiency and other defects in the film increases. It is apparent from the STEM and TEM measurements that the films are epitaxial, and the interface with the substrate is sharp and coherent. Nevertheless, the defect density is dependent on the background oxygen pressure during growth, with a lower defect concentration being observed when the film is grown in a higher oxygen background pressure. A high background oxygen pressure gives rise to biphasic thin films, as observed at room temperature. The high symmetry crystal phase (I type) corresponds to the crystal structure of the low oxygen pressure sample, in which symmetry considerations have been claimed to be incompatible with the long-range cation ordering. The second phase is

a lower symmetry state (P type) that might present B-site ordering. Consistent with the microscopy and EELS data, the Raman scattering results show that the AS mode shifts toward lower frequency, while the S mode shifts toward higher frequency, with increasing oxygen pressure as the film achieves a more bulklike structure. The magnetic moment of the samples increases and a sharpening of the ferromagnetic-paramagnetic transition is observed with increasing pressure, while the transition temperature (T_C) essentially remains unchanged. The failure to obtain the theoretical saturation magnetization of spin-only of $5\mu_B$/f.u expected for the fully ordered $La_2Ni^{2+}Mn^{4+}O_6$, even under optimized growth conditions, suggests that a low level of atomic disorder, primarily associated with oxygen vacancies, persists even in the films grown at the highest oxygen pressure. Based on Raman measurements, the critical thickness for strain relaxation is determined to be between 40 and 80 nm. However, the strain is found to have negligible influence on the magnetic properties. The results of the Raman, XPS, and EELS measurements suggest that the Mn and Ni ions in LNMO are mixed-valent Mn^{3+}/Mn^{4+} and Ni^{3+}/Ni^{2+}, and charge disproportionation of the $Mn^{4+}+Ni^{2+}\rightarrow Mn^{3+}+Ni^{3+}$ type likely occurs with decreasing oxygen pressure. The results of this study clearly indicates the importance of oxygen defects and mixed cation valence in determining the properties of the ferromagnetic double perovskite compound LNMO and the need to carefully control the process conditions in order to realize its intrinsic properties.

ACKNOWLEDGMENTS

This work was supported by ONR Grant No. N000140610226 (C. E. Wood) and NSF MRSEC Grant No. DMR-0213985. The Raman microscope was obtained via a DOE EPSCoR implementation grant (FG02-01ER45867). The work of M.N.I. was supported by the State of Texas through the Texas Center for Superconductivity at the University of Houston. The research at ORNL was sponsored by the Laboratory Directed Research and Development Program of ORNL, managed by UT-Batelle, LLC, for the U.S. Department of Energy under Contract No. DE-AC05-00OR22725. The FEI Titan was provided as part of the TEAM project, funded by the Division of Scientific User Facilities, U.S. Department of Energy. The authors wish to thank T. Calvarese and M. A. Subramanian for providing the ceramic LNMO target used for the growth of the thin films, and J. T. Luck for specimen preparation for the STEM measurements.

*agupta@mint.ua.edu

[1] M. Fiebig, T. Lottermoser, D. Fröhlich, A. V. Goltsev, and R. V. Pisarev, Nature (London) **419**, 818 (2002).
[2] T. Kimura, T. Goto, H. Shintani, K. Ishizaka, T. Arima, and Y. Tokura, Nature (London) **426**, 55 (2003).
[3] T. Lottermoser, T. Lonkai, U. Amann, D. Hohlwein, J. Ihringer, and M. Fiebig, Nature (London) **430**, 541 (2004).
[4] B. B. van Aken, T. T. M. Palstra, A. Filippetti, and N. A. Spaldin, Nat. Mater. **3**, 164 (2004).
[5] A. Sharan, J. Lettieri, Y. Jia, W. Tian, X. Pan, D. G. Schlom, and V. Gopalan, Phys. Rev. B **69**, 214109 (2004).
[6] N. Hur, S. Park, P. A. Sharma, J. S. Ahn, S. Guha, and S.-W. Cheong, Nature (London) **429**, 392 (2004).
[7] J. Wang, J. B. Neaton, H. Zheng, V. Nagarajan, S. B. Ogale, B. Liu, D. Viehland, V. Vaithyanathan, D. G. Schlom, U. V. Waghmare, N. A. Spaldin, K. M. Rabe, M. Wuttig, and R. Ramesh, Science **299**, 1719 (2003).
[8] C.-H. Yang, S.-H. Lee, T. Y. Koo, and Y. H. Jeong, Phys. Rev. B **75**, 140104(R) (2007).
[9] N. S. Rogado, J. Li, A. W. Sleight, and M. A. Subramanian, Adv. Mater. (Weinheim, Ger.) **17**, 2225 (2005).
[10] M. P. Singh, K. D. Truong, and P. Fournier, Appl. Phys. Lett. **91**, 042504 (2007).
[11] R. I. Dass and J. B. Goodenough, Phys. Rev. B **67**, 014401 (2003).
[12] P. Padhan, H. Z. Guo, P. LeClair, and A. Gupta, Appl. Phys. Lett. **92**, 022909 (2008).
[13] J. B. Goodenough, A. Wold, R. J. Arnott, and N. Menyuk, Phys. Rev. **124**, 373 (1961).
[14] G. Blasse, J. Phys. Chem. Solids **26**, 1969 (1965).
[15] K. Asai, H. Sekizawa, and S. Iida, J. Phys. Soc. Jpn. **47**, 1054 (1979).
[16] M. Sonobe and K. Asai, J. Phys. Soc. Jpn. **61**, 4193 (1992).
[17] N. Y. Vasanthacharya, P. Ganguly, J. B. Goodenough, and C. N. R. Rao, J. Phys. C **17**, 2745 (1984).
[18] V. L. Joseph Joly, P. A. Joy, S. K. Date, and C. S. Gopinath, Phys. Rev. B **65**, 184416 (2002).
[19] C. L. Bull, D. Gleeson, and K. S. Knight, J. Phys.: Condens. Matter **15**, 4927 (2003).
[20] J. Blasco, M. C. Sánchez, J. Pérez-Cocho, J. García, G. Subía, and J. Campo, J. Phys. Chem. Solids **63**, 781 (2002).
[21] R. I. Dass, J.-Q. Yan, and J. B. Goodenough, Phys. Rev. B **68**, 064415 (2003).
[22] H. Guo, J. Burgess, S. Street, A. Gupta, T. G. Calvarese, and M. A. Subramanian, Appl. Phys. Lett. **89**, 022509 (2006).
[23] C. H. Park and D. J. Chadi, Phys. Rev. B **57**, R13961 (1998).
[24] J. P. Maria, S. Trolier-Mckinstry, D. G. Schlom, M. E. Hawley, and G. W. Brown, J. Appl. Phys. **83**, 4373 (1998).
[25] M. P. Singh, C. Grygiel, W. C. Sheets, Ph. Boullay, M. Hervieu, W. Prellier, B. Mercey, Ch. Simon, and B. Raveau, Appl. Phys. Lett. **91**, 012503 (2007).
[26] L. Martín-Carrón and A. de Andrés, Eur. Phys. J. B **22**, 11 (2001).
[27] C. L. Bull and P. F. McMillan, J. Solid State Chem. **177**, 2323 (2004).
[28] M. N. Iliev, H. Guo, and A. Gupta, Appl. Phys. Lett. **90**, 151914 (2007); M. N. Iliev, M. V. Abrashev, A. P. Litvinchuk, V. G. Hadjiev, H. Guo, and A. Gupta, Phys. Rev. B **75**, 104118 (2007).
[29] L. Martín-Carrón, A. de Andrés, M. J. Martínez-Lope, M. T. Casais, and J. A. Alonso, Phys. Rev. B **66**, 174303 (2002).
[30] M. N. Iliev, M. V. Abrashev, V. N. Popov, and V. G. Hadjiev,

Phys. Rev. B **67**, 212301 (2003).
[31] A. Kowalcyzk, J. Baszyńki, A. Szajek, A. Ślebarski, and T. Toliński, J. Phys.: Condens. Matter **13**, 5519 (2001).
[32] D. D. Sarma, N. Shanthi, S. R. Barman, N. Hamada, H. Sawada, and K. Terakura, Phys. Rev. Lett. **75**, 1126 (1995).
[33] K. T. Ng and D. M. Hercules, J. Phys. Chem. **80**, 2094 (1976).
[34] P. E. Brommer and J. J. M. Franse, in *Ferromagnetic Materials*, edited by K. H. J. Buschow and E. P. Wohlfarth (North-Holland, Amsterdam, 1990), Vol. 5, p. 323.
[35] K. P. Poeppelmeier, M. E. Leonowicz, and J. M. Longo, J. Solid State Chem. **44**, 89 (1982).
[36] K. P. Poeppelmeier, M. E. Leonowicz, J. C. Scanlon, J. M. Longo, and W. B. Yelon, J. Solid State Chem. **45**, 71 (1982).